Theoretical Study of a Porous Silicon Cavity Based on Second Harmonic Waves Formed by Ferroelectric Crystals for Wide Range Multiphysical and Chemical Measurement

Jie Xu, Chu-Ming Guo, Cheng Yang, and Hai-Feng Zhang

***Abstract*— A metalayer (ML) composed of indium antimonide, ferroelectric crystals, and porous silicon (Psi) with high transmission, sensing properties, wide detecting range, and multiple physical measurements is proposed which is optimized by the improved ant colony algorithm (IACO). Due to the quasi-phase matching principle and nonlinear optical properties, the second harmonic waves (SHWs) with high conversion efficiency are successfully generated in the micrometer operating band and form a high and narrow transmission peak for sensing detection. Through analysis using the transfer matrix method (TMM) which is driven by IACO to accelerate the optimization of structures, the sensing performance sensitivity (S), quality factor (Q), figure of merit (FOM), and detection limit (DL) are calculated. The proposed ML demonstrates the capability to measure thickness (S = 18.75, Q = 11 885, FOM = 332 μm^{-1}), external temperature (S = 4.6 nm/K, Q = 7046, FOM = 0.049 K^{-1}), and magnetic field intensity (S = 1332 nm/T, Q = 8146, FOM = 16.3 T^{-1}). Additionally, it exhibits an ultrawide refractive index (RI) sensing range from 1 to 5, and excels in detecting hydrobacteria, and viruses with good sensing performance (S = 44 000 and 43 460 nm/RIU), high Q values (5585 and 6103), and low DL (1.38 × 10^{-4} and 1.3 × 10^{-4} RIU). This versatile and promising ML design offers possibilities for comprehensive multiphysical and chemical parameter measurements in diverse fields.**

***Index Terms*— Ant colony optimization (ACO), ferroelectric crystal, metalayer (ML), multiphysical and chemical quantity wide range measurement, second harmonic wave (SHW) generation.**

I. Introduction

THE metalayer (ML) is a material characterized by a periodic distribution of dielectric constants and refractive indices (RIs), holding significant importance within the realm of photonics. It is composed of various layers of media meticulously arranged in a specific spatial order. This unique structural configuration and composition give rise to intriguing optical phenomena, involving the diffraction and interference of light waves within its confines. Within a defined frequency range, corresponding to specific wavelengths is associated with the creation of a photonic band gap (PBG). These fundamental characteristics underpin resonance and phase modulation, ultimately leading to the acquisition of distinctive and valuable physical properties [1], [2]. Comprising various stacked material layers forming a periodic structure, ML exhibits unique PBG and energy local physical characteristics [3], [4], [5], enabling the design of optical waveguides, filters, and converters through Bragg scattering of electromagnetic waves (EWs) [6], [7], [8]. Optical sensors, known for their non-contact nature, high sensitivity (S), fast response, and low power consumption, serve as vital detection tools, with ML being widely utilized in their design [9]. These sensors rely on optical principles to detect diverse physical and chemical quantities in the environment, converting interactions with light waves into electric signals, and then processing the results for visible display, making them prevalent in photoelectric, optical fiber, and optical imaging sensors [10]. The proposed ML, based on the intrinsic resonance principle of indium antimonide (Insb), belongs to the class of optical cavity sensors in the realm of optical spectral sensors [11]. By incorporating layered Insb, the overall structure gains intrinsic resonance characteristics, aligning the intrinsic vibration of material with the incident wavelength of EWs at specific frequencies [12]. This leads to a heightened transmittance of light at that wavelength as it passes through the structure. Currently, many ML sensing designs are available. A temperature sensor was proposed by Kumar et al. [13]. A bio-alcohol sensing ML structure was proposed by Al-Dossari et al. [14]. However, these designs often lack consideration for multiphysical and chemical quantity detection and wide-range measurement capabilities. Many sensing designs can only detect a single physical quantity, limiting the utilization efficiency of the ML. Moreover, the measurement range is often confined to the vicinity of the target object, which can negatively impact the measurement

Manuscript received 3 November 2023; revised 29 February 2024; accepted 12 March 2024. Date of publication 25 March 2024; date of current version 4 April 2024. This work was supported in part by the National College Students Innovation and Entrepreneurship Training Program under Grant 202310293015Z and in part by the College Student Innovation Training Program of Nanjing University of Posts and Telecommunications. The Associate Editor coordinating the review process was Dr. Javad Gatabi. *(Corresponding author: Hai-Feng Zhang.)*

The authors are with the College of Electronic and Optical Engineering and the College of Flexible Electronics (Future Technology), Nanjing University of Posts and Telecommunications, Nanjing 210023, China (e-mail: hanlor@163.com).

This article has supplementary downloadable material available at https://doi.org/10.1109/TIM.2024.3381724, provided by the authors.

Digital Object Identifier 10.1109/TIM.2024.3381724

function of sensors if the physical data of the detected object deviates from this narrow range. Therefore, a need exists for more comprehensive and versatile ML designs capable of detecting multiple physical quantities across a broader range.

In recent years, nonlinear optics has been an active area of research, showcasing distinctive effects in special materials with high intensity and energy density, encompassing optical frequency mixing, phase modulation, and self-focusing [15], [16], [17]. ML with nonlinear polarization media change has generated numerous scientific phenomena, such as optical bistability and PBG drift, through their combination of PBG and nonlinear optical effects [18], [19]. A central focus of this study is second harmonic wave (SHW) generation, wherein incident light passing through nonlinear materials leads to nonlinear polarization, resulting in some energy being absorbed by another group of photons, generating a resonance frequency twice that of the incident light [20], [21]. Moreover, periodically altering the polarization direction and thickness in nonlinear ML significantly affects photon-electron or photon-molecule interactions. Periodically polarized ferroelectric crystals (PFC) are widely employed as nonlinear materials subject to thermal and magnetic control, further optimizing SHW generation, as researchers continue striving to enhance nonlinear Conversion efficiency (T-con) for improved SHW applications [22], [23]. Traditional SHW research only focuses on the generation mechanism of SHW and the influence of the corresponding structural parameter setting on T-con and does not further study the special physical characteristics brought by SHW. In this article, the high transmission peak generated by SHW is used for sensing and detection, and the utilization of SHW is expanded.

Porous silicon (Psi) has been widely employed in the design of ML owing to its significant advantages [24]. The unique properties of Psi, such as aperture control and versatile surface chemistry, allow for precise adjustment of the refractive index (RI) of the filler, making it highly versatile in various research fields [25]. Particularly in gas, chemical, and biological analysis, its capacity to finely tune the effective RI grants its high S to even minute changes. When combined with a gas cavity, it facilitates the creation of an analyte layer for filling, leading to a well-suited multilayer stack structure for the design conditions of the sensor. The analytes in this article can be continuously replaced by filling the structure composed of Psi to realize the analysis of more detected substances. Psi is conventionally generated through the electrochemical anodization of crystalline silicon within a hydrofluoric acid solution. The porosity of the resulting structure is determined by the current density applied during the anodic oxidation process, representing the volumetric proportion of pores within the material [26]. Notably, the electrochemical etching procedure is inherently self-limiting in nature. It exclusively transpires at the boundary interface between the Psi layer and the underlying crystalline silicon substrate. Consequently, previously etched porous regions remain unaffected by subsequent electrochemical etching processes. This method is characterized by its expeditiousness and cost-effectiveness.

Artificial intelligence is one of the most popular types of research at present, among which optimization algorithm also occupies a place. Optimization algorithm, as the most basic program theory, brings great convenience to computer calculation. Ant colony optimization (ACO) is an optimization technique that can be called artificial intelligence ant inspired by the foraging behavior of ant colonies in nature [27]. It was originally proposed and applied by Italian mathematician Marco Dorigo in the early 1990s, and subsequent researchers have further developed and refined it [28]. ACO is rooted in the behaviors exhibited by ants in their search for food, and they are harnessed for solving complex optimization problems. In this algorithmic framework, each individual ant represents a potential solution to the problem at hand. These ants traverse the problem space, effectively charting out potential solution paths. First, the concentration of pheromones along a path serves as an indicator of path quality. Ants exhibit a preference for paths with higher pheromone concentrations, interpreting these as better choices. And then, heuristic information plays a pivotal role. It typically represents the heuristic estimation made by an ant from its current location to the target location. This information guides ants in their path selection. As ants move along their chosen paths, they deposit pheromones based on the perceived quality of the path. Paths of superior quality release more pheromones. Over time, these pheromones naturally evaporate. However, the choices made by ants continually refresh the pheromone concentrations. Through numerous iterations, the ant population gradually converges toward an optimal solution, allowing them to uncover the best or near-best solutions to the problem at hand. Notably, the elite ant system and the largest and smallest ant system are commonly used variations of the algorithm [29], [30]. In this study, an adaptive ant colony algorithm is employed to enhance the transfer matrix method (TMM) for analyzing the physical properties of ML [31], [32], [33]. By using TMM, the absorption and transmission rates of EWs through the structure can be calculated and analyzed. Previously, the complex matrix operations of TMM and the abundance of variables in ML design made it challenging to optimize the structure, often relying on time-consuming enumeration trial-and-error methods. In this article, an improved ACO (IACO) is utilized to optimize the structural design of ML [34]. The IACO streamlines the matrix operations in TMM, increasing the speed of high-dimensional operations and reducing the time required for the structural design process. ACO is currently one of the most widely used optimization algorithms, and it possesses several distinctive advantages. Notably, its optimization methodology is rooted in distributed computation, enabling multiple individuals to compute in parallel. IACO inherits these strengths while adding further robustness. When confronted with intricate, nonlinear, and multimodal optimization challenges, it excels and exhibits a heightened ability to navigate such complexities, making it particularly well-suited for high-dimensional matrix operations. Furthermore, the algorithm demonstrates adaptability in its operations. Ants, the agents within the algorithm, dynamically adjust their behavior in response to fluctuations in pheromone concentration along their paths. This adaptability renders the ant colony algorithm highly resilient in the face

of evolving environmental conditions and problem dynamics, making it a robust choice for a wide range of optimization scenarios. Generally speaking, the proposed ML has a high transmittance in the micrometer operating band. The designed ML can be applied in optical sensor applications, providing measurement and monitoring functions for thickness, external temperature (T_{ext}), magnetic induction intensity (B), as well as detecting hydrobacteria and viruses. Thanks to the quasi-phase matching principle, the resonant mode remains relatively stable, ensuring a wide measuring range of RI in the analyte-filled layer composed of air and Psi. The superiority of the IACO algorithm grants the sensor a high S, quality factor (Q), figure of merit (FOM), and a low detection limit (DL). In addition, it should be stated that the proposed ML only considers purely theoretical research, and specific experimental fabrication research is not within the scope of consideration in this article.

II. Theoretical Design of ML

A. Composition of Proposed Structure

The proposed ML structure, designed for the detection of multiple physical quantities and featuring a wide measurement range, consists of 18 layered structures arranged as $(PFC_2\text{-}Ko\text{-}Psi_1\text{-}Psi_2\text{-}In\text{-}PFC_1)^3$, as illustrated in Fig. 1(a). The dark blue dielectric layer represents the PFC_2 layer, which serves as the incident surface layer. In represents the Insb layer with a thickness of d_{Insb}, and Ko represents the air layer. d_{psi1} and d_{psi2} on behalf of the different thicknesses of Psi. The cavity layer has a thickness of d_{gas}, and the corresponding RI (n_{gas}) is determined by the filling medium. The cavity, enclosed by the orange solid wire square on the lower left side of Fig. 1(a), constitutes the analyte layer. The structure consists of two Psi layers, Psi_1 and Psi_2, along with air layers with different porosities, creating a structure capable of interacting and circulating with each other. The analyte placement structure is flanked by the dielectric PFC_2 layer on one side and the Ko layer on the other. These two media act as partitions in the filling layer, effectively insulating the analyte and preventing it from significantly impacting the overall physical properties of the structure. In Fig. 1(b), a schematic depiction of the sensing mechanism is illustrated from a planar perspective of the proposed structure. PFC_2 and PFC_1 serve as substrate materials at both ends, and analytes are introduced into the central region of the packaging structure to fill the cavity formed by Ko, Psi_1, and Psi_2. Notably, in the application of biosensing to differentiate cancer cells from normal cells and detect waterborne bacteria in a solution, RI sensing is executed by injecting analytes into an analytical layer. This is achieved through a micropermeation technology utilizing a hollow submicrometer-sized pipette, a precision technique as documented in [35]. The etching method is a common method used to prepare ML, which forms periodic structures by chemically or physically etching the surface of the material [36]. Detailed preparation methods are presented in Section 2 of Supplementary Material. In Fig. 1(a), the green apple cylinder indicates the incident direction of the EWs, with an angle of θ relative to the horizontal direction.

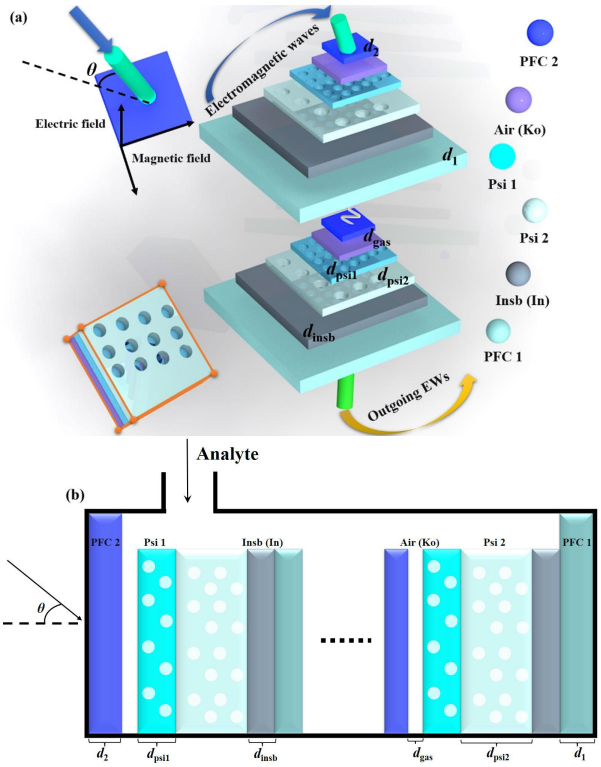

Fig. 1. (a) Design sensing structure of the proposed ML and (b) working design of sensing purposes.

The incident wave propagates as a transverse magnetic (TM) wave mode, with the magnetic field direction perpendicular to the EWs propagation direction and horizontally distributed along the structure surface. Notably, this study focuses on exploring SHW generation, necessitating an investigation of the physical properties of the proposed ML under both fundamental wave (FW) and SHW conditions. In Fig. 1(a), the layered $LiNbO_3$ materials denoted as PFC_2 and PFC_1, have thicknesses d_1 and d_2, respectively. Their fundamental frequency RIs are nf_1 and nf_2, while their frequency multiplier RIs are np_1 and np_2, influenced by the applied electric field. The specific formulas for these parameters are provided below [20]

$$np_1 = nf_1 + \Delta np_1 = nf_1 - \frac{1}{2} nf_1^3 r_{33} E \tag{1}$$

$$np_2 = nf_2 + \Delta np_2 = nf_2 + \frac{1}{2} nf_2^3 r_{33} E. \tag{2}$$

The electro-optical coefficient, denoted as r_{33}, corresponds to the specific material's properties, and E represents the amplitude of the electric field. These parameter settings are analogous to nonlinear coefficients, and the value of r_{33} holds distinct significance in various research domains. The FW RIs, nf_1, and nf_2, are obtained using the following formula [20]:

$$nf = O + \frac{U}{\lambda^2 - V^2} - W\lambda^2. \tag{3}$$

The values of parameters U, O, V, and W vary under different environmental settings. The specific definition of each parameter is referred to [40]. In the ML design structure, their values are set as: $U = 5.065$, $O = 11.13 \times 10^4$, $V = 6.7525 \times 10^4$, and $W = 1.605 \times 10^{-5}$, respectively [20]. It is

worth noting that the RI setting of nf_1 and nf_2 is artificially controlled, and the electro-optical control of PFC_1 and PFC_2, as a special material, can effectively manipulate the optical signal, thus providing a foundation for SHW production in combination with the nonlinear Kerr effect. Therefore, the dielectric constant of the PFC material can be expressed as follows [37]:

$$\varepsilon = \varepsilon^{NL} + \varepsilon^{\mathrm{L}} = \varepsilon^{\mathrm{L}} + \varepsilon_0 \chi E^2 \tag{4}$$

where the linear and nonlinear permittivity of the medium is represented by L and NL, respectively. The nonlinear permittivity is further expanded as the product of the nonlinear polarizability χ, the permittivity in vacuum ε_0, and the surrounding electric field E. This equation is combined with the continuity equation of particle transport [38]

$$\frac{\partial \rho_e}{\partial t} + \nabla(\Gamma_e \rho_e E - F \nabla \rho_e) = \rho_e \upsilon_e \alpha(E, P) - S_e \tag{5}$$

where the definition in the above formula can be referred to the [38]. Through (5), the permittivity of PFC_1 and PFC_2 can be further obtained by considering the electron density (ρ), electron diffusion coefficient (F), electron ionization coefficient (α), and electron loss rate (S_e) [38]

$$\varepsilon_{\mathrm{PCF}} = 1 - \frac{e^2 \Gamma_e E \alpha(\mathrm{EP})}{\varepsilon_0 m_e \beta \omega^2 (1 + j\upsilon_m/\omega)}. \tag{6}$$

With the propagation of EWs in the structure, the dielectric constant of each layer of PFC is influenced by the internal electric field distribution E in the large periodic arrangement structures, resulting in a highly complicated calculation process. To simplify the calculation process, the amplitude distribution of the continuous wave differs significantly from the signal amplitude under the condition of high incident light intensity is considered into. Thus, the nonlinear correction term caused by the signal wave can be neglected in the calculation process [39]

$$npf = np + \Delta npf \cdot I. \tag{7}$$

Here the intensity of the control wave is denoted by I, and np stands for the initial value of the RI of PFC_1 and PFC_2 under the condition of the SHW. The final RI value npf is approximated using the optical Kerr effect under continuous EWs excitation.

Similarly, as a widely used material, the dielectric constant formula of Psi differs from that of ordinary media. Before calculating the dielectric constant of Psi, it is essential to determine the characteristics of silicon RI as it changes with the working wavelength [40]

Then, let [26]

$$n_{\mathrm{psi}} = 0.5\sqrt{M + \sqrt{M^2 + 8n_{si}^2 n_{\mathrm{gas}}^2}} \tag{9}$$

$$M = 3P\left(n_{\mathrm{gas}}^2 - n_{si}^2\right) + \left(2n_{si}^2 - n_{\mathrm{gas}}^2\right). \tag{10}$$

In the provided description, n_{psi} represents the final RI, n_{gas} stands for the RI of the object injected into the hole, and M signifies the porosity of the Psi and the influence of the packed analyte on the overall RI value. In the investigation of ML, crucial physical quantities such as absorption rate (A), reflectance (R), and transmittance (T) are taken into consideration. Owing to the intricacy of model construction and the multidimensional nature of calculations, the TMM is employed to calculate the correlation matrix. However, due to the generation of SHW and the incorporation of nonlinear materials, enhancements have been made to TMM to ensure more precise calculations. Next, the calculation of TMM under SHW condition is derived by Maxwell's equations are presented in Section 1 of Supplementary Material [41].

B. Sensing Performance Evaluation Method

In the application of the proposed ML for sensing, to facilitate a clear comparison of the sensor's performance, researchers have defined S, Q, FOM, and DL. These parameters are categorized into the frequency domain and wavelength domain, based on the differences in calculation formulas for different research domains. For this article, the wavelength domain is the focus of investigation [44]

$$S = \frac{\Delta\lambda}{\Delta x} \tag{11}$$

$$Q = \frac{\lambda_T}{\mathrm{FWHM}} \tag{12}$$

$$\mathrm{FOM} = \frac{S}{\mathrm{FWHM}} \tag{13}$$

$$\mathrm{DL} = \frac{\lambda_T}{20SQ} \tag{14}$$

where λ denotes the working wavelength, Δ represents the variation in value, S signifies the relationship between the change in the detected quantity and the corresponding wavelength displacement, λ_T stands for the peak wavelength, and FWHM is the wavelength difference at half of the peak.

C. Calculation Method of IACO

The proposed IACO is employed to drive the TMM calculation and optimize the ML structural model, as outlined in Fig. 2. The ACO algorithm emulates the foraging behavior of ants, applying mathematical formula fitting to concretize the abstract phenomenon in the animal world. Before initiating the calculation, a series of parameters are set. Initially, W ants are randomly placed in the city, and the initial pheromone values on each path are made equal. Since the sensing performance in this article is represented as a transmission peak, each city depicts a transmission peak. The initial pheromone value is set as [45]

$$\tau_{ij}(0) = \tau_0 \tag{15}$$

$$\tau_0 = \frac{W}{L_W} \tag{16}$$

where τ_0 stands for the value of the initial pheromone and L_W denotes the path length constructed by the nearest neighbor heuristic. Different routing means different parameter settings. Subsequently, for ant kk ($kk = 1, 2, \ldots, W$), the next city to be transferred is selected based on the random proportion rule, and its selection probability is determined by the following

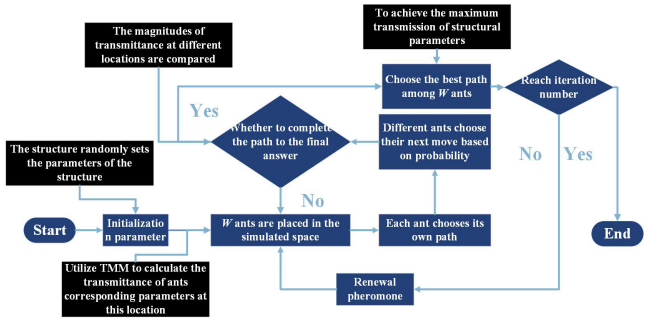

Fig. 2. Process of IACO utilizes TMM to optimize.

expression:

$$\zeta_{ij}^{kk}(t)=\begin{cases}\dfrac{[\tau_{ij}(t)]^{\alpha}[\gamma_{ij}(t)]^{\beta}}{\sum_{s\in a^{kk}}[\tau_{is}(t)]^{\alpha}[\gamma_{is}(t)]^{\beta}}, & \text{if } j\in a^{kk}\\ 0, & \text{Others}\end{cases}\tag{17}$$

where τ represents the pheromone level on the edge between city i and city j, while γ denotes the heuristic factor indicating the attractiveness of moving from city i to city j. The set a^{kk} stands for the cities that ant kk will be allowed to visit next. α and β are two constants, respectively, the weight value of pheromone and visibility

$$\tau_0=\frac{W}{L_W}.\tag{18}$$

Here, the variable ζ has a range of (0, 1) and depicts the evaporation rate of the pheromone. In the general problem, the value of ζ is commonly set to 0.5. Additionally, $\Delta\tau_{ij}^{k}$ represents the pheromone level left by ant k on the path

$$\Delta\tau_{ij}^{kk}=\begin{cases}(C_{kk})^{-1}, & \text{if the } k\text{th ant traverses}(i,j)\\ 0, & \text{others}\end{cases}\tag{19}$$

where C_k stands for the total path length obtained by the kth ant after completing the entire path. As per (19), when the ants construct shorter paths, they accumulate more pheromones on each edge of the path, increasing the likelihood of being chosen by other ants in future iterations. Upon completing a cycle, the ant clears its tabu table and returns to the original city, preparing for the next trip.

While the basic algorithm performs well in low-dimensional cases with few parameter settings and can quickly find optimal paths, it faces challenges as the construction model becomes more complex, leading to performance deterioration and noticeable stagnation. To address these issues, this article proposes an IACO method. The key to this enhancement lies in how pheromones are updated, allowing for more efficient exploration of the search space and better convergence toward optimal solutions [46]. In this context, it is important to provide a detailed explanation of the concept of the search space as it applies to the algorithmic aspect of our study. In algorithmic terms, we can liken the search space to a map where virtual ants are seeking optimal solutions, much like real ants searching for food. In our physical application, this search space is a representation of countless points, each denoting a specific physical property corresponding to various optimization parameter settings. This expansive map encompasses the entire range of potential configurations, allowing us to explore and identify better conditions for our research

$$\begin{cases}\tau_{ij}(t+1)=(1-\xi)^{1+\varphi(W)}\cdot\tau_{ij}+\Delta\tau_{ij}, & \tau\geq\tau_{\max}\\ \tau_{ij}(t+1)=(1-\xi)^{1-\varphi(W)}\cdot\tau_{ij}+\Delta\tau_{ij}, & \tau<\tau_{\max}.\end{cases}\tag{20}$$

The proposed IACO employs a combination of deterministic and random selection strategies to enhance convergence efficiency. The number of continuous convergences, denoted as W, is used as a function proportional to the convergence count. A higher number of convergences W leads to a greater value of $\varphi(W)$. During the search process, the probability of deterministic selection is dynamically adjusted in real time. Once the evolution direction is largely determined after reaching a certain number of convergences, the information on the paths is dynamically adjusted to narrow the gap between the best and worst paths. This ensures a more balanced distribution of information and allows for a more comprehensive search of the solution space.

When dealing with ML design models that involve numerous parameters or layers, and complex high-latitude matrix operations are required by TMM, the existence of an information volatilization coefficient reduces the amount of information on paths that have not been explored to nearly zero. This prevents ants from repeatedly choosing the same path. Conversely, paths with a large amount of information are more likely to be selected again, potentially affecting the algorithm's ability to find a better solution. In such cases, adjusting the volatilization coefficient helps control the convergence speed of the algorithm.

By dynamically adjusting the information intensity on each path based on the solution distribution, the movement of ants is neither too concentrated nor too scattered, thus avoiding premature convergence and local optima. As a result, the global search ability of the algorithm is enhanced, and the model parameters can be adjusted with greater precision. This optimization strategy improves the overall efficiency and effectiveness of the proposed ACO method in designing ML.

III. Design and Simulation Results

After constructing the 18-layer ML, the sensing performance and its wide measurement range are obtained by optimizing the thickness of each layer medium (d_1, d_2, d_{psi1}, d_{psi2}, d_{Insb}, d_{gas}), the dielectric constant of Insb under T_{ext} and B, the porosity of silicon (k_{psi1}, k_{psi2}), and light intensity (I_t).

$$n_{si}=\sqrt{\left(1+\frac{10.6684293\lambda^2}{\lambda^2-0.301516485^2}+\frac{0,0030434748\lambda^2}{\lambda^2-1.13475115^2}\right)+\frac{1.54133408\lambda^2}{\lambda^2-1104^2}}.\tag{8}$$

TABLE I
ALL PARAMETERS TO BE OPTIMIZED

IACO	Parameter	range	unit	Optimization result
Parameters to be optimized	d_1	10~10^4	nm	5.803 μm
	d_2	10~10^4	nm	0.602 μm
	d_{psi1}	10~10^4	nm	22.9 nm
	d_{psi2}	10~10^4	nm	63.8 nm
	d_{Insb}	10~10^4	nm	7.04 μm
	d_{gas}	10~10^4	nm	7.36 μm
	θ	0~89	°(degree)	0°
	k_{psi1}	0~1	None	0.43
	k_{psi1}	0~1	None	0.865
	B	0~2	T	0.05 T
	I_t	10^3~10^5	GW/cm^2	30.9106×10^3 GW/cm^2
	T_{ext}	200~400	K	300 K

The incident angle of EWs θ is also optimized utilizing the IACO. The details of the parameters to be optimized can be seen in Table I.

Furthermore, certain parameters are held constant in the study. The RIs n_{gas}, n_{psi1}, and n_{psi2} are set to 1 when no analyte is added. Regarding the PFC setting, the nf_1 and nf_2 are assigned values of 1.617 and 2.955, respectively [42]. Additionally, the np_1 and np_2 are set to 1.68 and 3.245. The third-order nonlinearity, represented by χ_3, is defined as 27.2 pm·v^{-1}. Based on the given data, the ML is designed accordingly. When the EWs are vertically incident from the PFC_2 layer, a sharp transmission peak is obtained, as illustrated in Fig. 3(a). A high transmittance of 99.9% at the operating wavelength of 665.76 μm is achieved by ML. The requirement of sensing performance being above 0.9 is met, ensuring sensing capabilities, meaning that the sensing performance is not affected by other signals during operation.

The structure outlined in this article is capable of producing high-quality transmission peaks within the respective operating frequency range. This phenomenon arises from the precise adjustment of dielectric layer combinations and thicknesses, allowing resonance to occur at specific wavelengths. This optical resonance significantly enhances the transmission of wavelengths through the optical fiber. Moreover, the successful generation of SHW results in a doubling of the resonance frequency, further enhancing the quality and amplitude of these transmission peaks. Building upon this foundation, our proposed structure is extended for the purpose of substance detection. This extension relies on the impact of the analyte on the transmission spectrum of the proposed structure. By observing alterations in the transmission peak, we can effectively demonstrate the sensing capability for detecting changes in the measured substance.

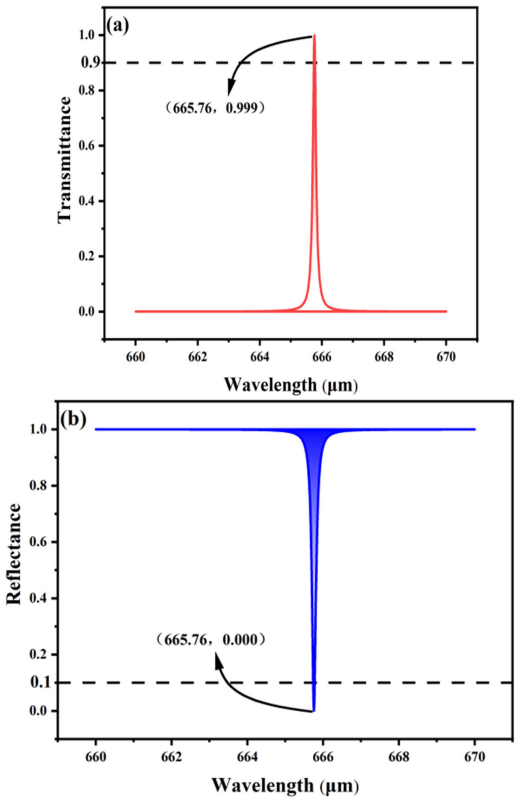

Fig. 3. (a) Transmission peak generated by ML based on SHW during forward propagation of EWs. (b) Reflection peaks generated by ML based on SHW during EWs backward propagation.

To further support the notion that the transmittance peak is induced by the intrinsic resonance of the Insb layer, Fig. 3(b) displays the scenario where EWs are incident from the PFC_1 dielectric layer behind the structure. Obviously, a low reflectance is observed at the operating wavelength of 665.76 μm, nearing 0. The similarity in shape and change between the transmittance peak generated by forward incidence and the reflection peak generated by reverse incidence, along with their shared peak value at the same wavelength point, indicates that the intrinsic resonance formed by the Insb layer significantly influences the propagation of EWs throughout the entire proposed ML, thereby resulting in alterations to the transmittance of EWs.

In comparison to FW, EWs offer several advantages in propagation, notably its signal amplitude enhancement feature, which improves sensing performance while simultaneously increasing frequency and decreasing wavelength. To provide evidence for the generation of SHW, Fig. 4(a) and (b) have been employed. Compared with Fig. 3(a) and (b), the central wavelength of the transmission peak and inverted reflection peak produces significant waveform changes, it is evident that the intrinsic resonance wavelength undergoes a transformation from 665.6 to 1585.2 μm, resulting in a relationship of 0.42 times between the two values. Additionally, the peak value shifts from FW to SHW, leading to a 196% increase in transmittance, thereby substantiating the generation of SHW.

SHW is highly tunable, allowing for the adjustment of SHW signal frequency and intensity by manipulating the parameters

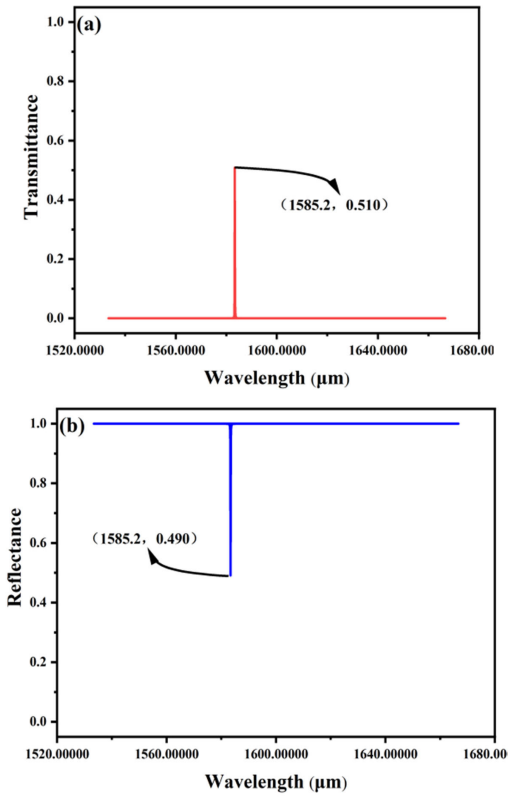

Fig. 4. (a) Transmission peak generated by ML based on FW during forward propagation of EWs. (b) Reflection peaks generated by ML based on FW during EWs backward propagation.

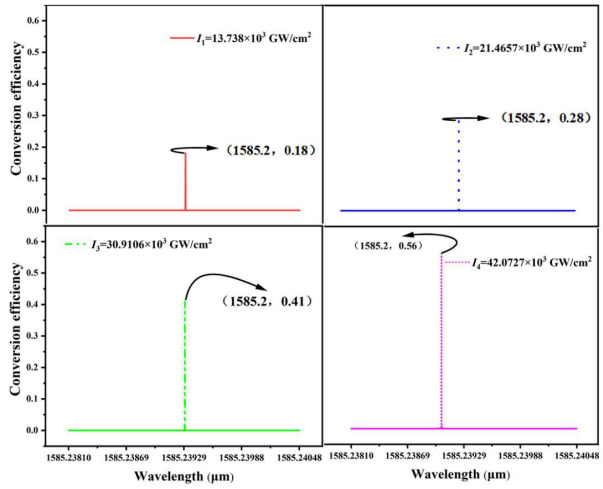

Fig. 5. Relationship between T-con and I_t when the FW is converted to SHW.

of the nonlinear system. This tunability makes it remarkably versatile in various applications. As depicted in Fig. 5, as I_t increases from 13.738×10^3 GW/cm^2 to 42.0727×10^3 GW/cm^2, the T-con exhibits significant variation, initially starting at 0.18, then progressing to 0.28, 0.41, and ultimately reaching 0.56.

Prior to discussing the sensing performance, a thorough exploration of the magnetic field distribution in the proposed ML is conducted to further substantiate the presence of transmission peaks, as presented in Fig. 6. The investigation

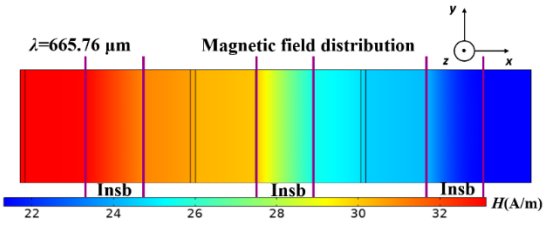

Fig. 6. Magnetic field distribution map of proposed ML.

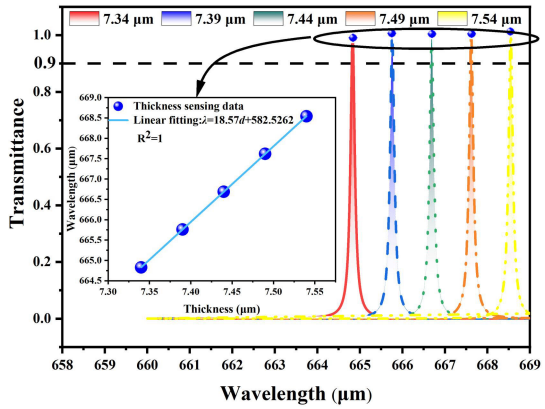

Fig. 7. Proposed ML corresponds to the shift of transmission peaks and the functional relationship between the peaks when detecting the thickness of d_{gas}.

revealed significant changes in the magnetic field within the Insb dielectric layer. Specifically, the region on the left side transitioned from deep red to red-orange, the middle section of the structure shifted from yellow-orange to green apple, and the right region altered from sky blue to sea blue, all corresponding to the Insb dielectric layers. These observations demonstrate the impact of intrinsic resonance on the magnetic field distribution throughout the entire ML.

The proposed ML exhibits not bad thickness sensing performance. Specifically, the air layer serves as the target for measurement, and any change in the thickness of d_{gas} directly affects the shift in the transmission peak, as depicted in Fig. 7. As the thickness increases from 7.34 to 7.39, 7.44, 7.49, and 7.54 μm, represented by the colors red, blue, green, orange, and yellow, respectively, the transmittance remains consistently near 0.99, with fluctuations not exceeding 5%. Furthermore, the peak wavelength consistently shifts toward higher values with increasing thickness, establishing a positive correlation. To explore the relationship between thickness and peak wavelength, each peak value is marked with a blue ball, and its corresponding x-coordinate value is recorded. The relationship is presented in Fig. 7.

The peak wavelengths are measured as 664.75, 665.704, 666.632, 667.538, and 668.489 μm as the thickness increases from small to large. By applying linear fitting to the discrete data points, a highly correlated positive correlation function with a strong correlation coefficient $R^2 = 1$ is obtained

$$\lambda = 18.57 d_{\text{gas}} + 582.5262. \tag{21}$$

With the phase relation value set at 1, the equation can be expressed as a linear equation. By using (11), the absolute

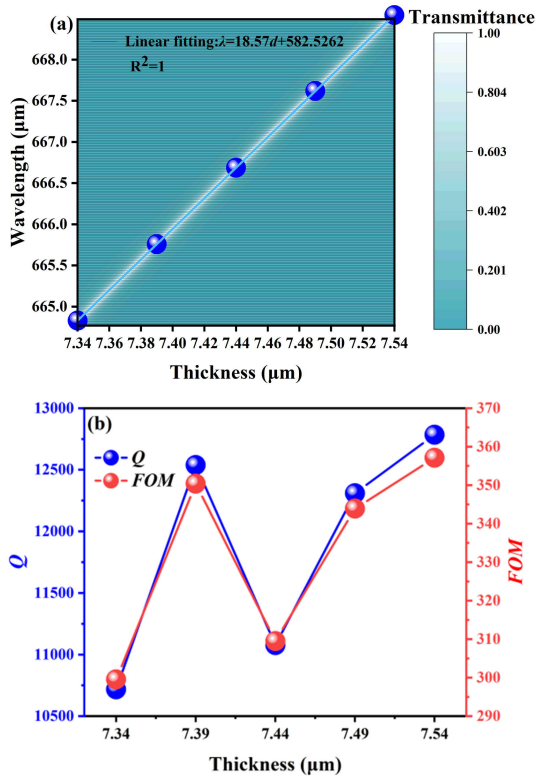

Fig. 8. Within the full thickness measurement range (a) transmittance distribution corresponding to each operating wavelength and (b) change curve of the sensing performance index.

value of the slope represents the magnitude of S in the relationship between the detected quantity and the peak wavelength. Then, by combining with (21), the value of S is determined to be as high as 18.57.

Fig. 7 provides evidence of a strong linear relationship at the selected discrete data points, but it does not establish the thickness sensing performance of the proposed ML across the entire measurement range. To address this limitation and avoid random data selection, a comprehensive analysis of transmittance throughout the entire thickness measurement range (from 7.34 to 7.54 μm) is conducted in the operating wavelength domain. The results are shown in Fig. 8(a), where the white gradient to cyan color indicates a decrease in transmittance from 1 to 0. Around 95% of the figure is represented by the cyan distribution, and a single white line runs through the entire icon. This white line indicates that there is transmittance greater than 0.99 at each thickness set point and the fit curves in Fig. 7 overlap. Fig. 8(b) is used to demonstrate the thickness sensing performance. By utilizing (12) and (13), the performance index is calculated for the selected data points. The average values for Q and FOM are 11 885 and 332 μm^{-1}, respectively, with a consistent overall growth trend. The minimum values of 10 718 and 299.5 μm^{-1} start to rise, reaching a peak value of 12 538 and 350 μm^{-1}. Subsequently, they experience a brief decline before rising again at different rates to a maximum of 12 784 and 357 μm^{-1}.

Fig. 9 demonstrates the application of the same calculation method for thickness sensing. Different T_{ext} settings are explored, and the shift of transmission peaks is observed,

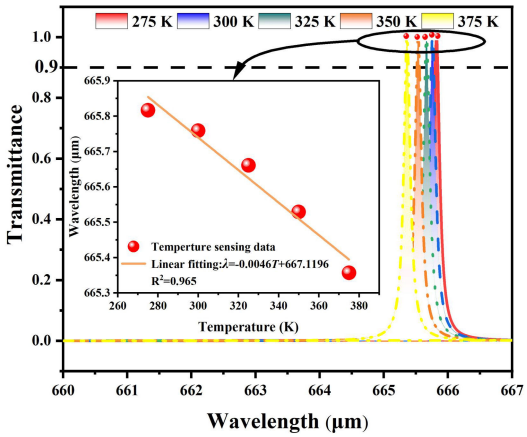

Fig. 9. Shift of the transmission curve with a change of T_{ext} and the relationship between the peak wavelength and the T_{ext} setting.

with corresponding peak values represented by different colors. Specifically, the red straight line corresponds to 275 K, resulting in a peak wavelength of 665.817 μm, while the deep blue dashed line is 300 K, leading to a peak wavelength of 665.759 μm. Likewise, the teal dotted line stands for 325 K, producing a peak wavelength of 665.661 μm, the orange dash-dotted line on behalf for 350 K, resulting in a peak wavelength of 665.529 μm, and the yellow double-dash-dotted line corresponds to 375 K, yielding a peak wavelength of 665.357 μm. Throughout the T_{ext} range, the shifting trend of peak wavelengths changes from right to left. Remarkably, the transmittance achieves an impressive 99.9%, almost reaching 100% transmission. Further analysis of the peak values reveals a quasi-linear relationship between peak wavelength and T_{ext}. Data fitting is conducted, leading to a fit function that highlights the negative correlation between wavelength and T_{ext}. For the sensing function of a structure, it is necessary that the change of the amount of change and the change of the peak corresponding to the central wavelength meet the linear relationship

$$\lambda = -0.0046d + 667.1196. \tag{22}$$

The high correlation coefficient of 0.965 indicates a strong relationship between the x- and y- axes. The S is quantified at 4.6 nm/K, meaning that each 1 K change in T_{ext} corresponds to a 4.6 nm shift in peak wavelength. T_{ext} sensing covers a broad measurement range of 275 to 375 K, corresponding to T_{ext} ranging from 2 °C to 102 °C, encompassing typical T_{ext} variations. The curve fitting of the selected data points has a certain chance, which can only represent a strong linear relationship between the peak wavelengths at the five data points of 275, 300, 325, 350, and 375 K. In order to explain the whole temperature measurement range more comprehensively, this functional relationship still exists, and further data processing is carried out. In the whole range from 275 to 375 K, whether the change of the central wavelength and temperature of the transmission peak accord with the fitting curve and whether there is a high transmission value.

In Fig. 10(a), the watermelon color scheme is utilized to illustrate the distribution of transmittance in a 2-D image comprising peak wavelength and T_{ext}. The color spectrum ranges

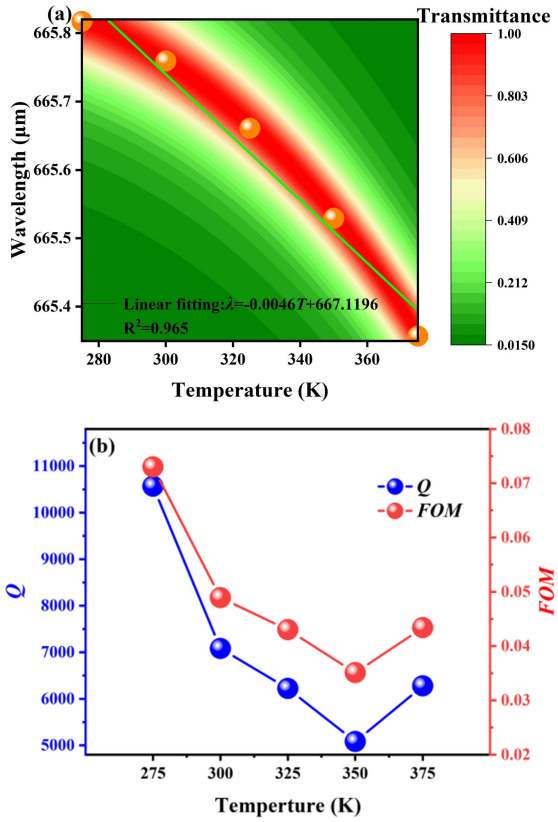

Fig. 10. (a) Distribution of transmittance in a 2-D relationship consisting of the entire T_{ext} and operating wavelength. (b) Performance indicators of T_{ext} sensing.

from dark red, representing high transmittance, to green, indicating low transmittance. Most of the color filling is occupied by green, indicating that after removing the high transmission in the middle section, there are a few high transmission values and most low values in a certain temperature in the whole working band, and the distribution is consistent with the peak distribution in Fig. 9. Notably, the dark red curve is prominently positioned in the middle of the figure, covering approximately 20% of the entire interface. The wider part of the dark red curve signifies that the transmission peak curve is broader under specific T_{ext} settings. To represent the discrete data points, orange stereo spheres are strategically placed on the plot, aligning with the overall trend of the dark red curve. Subsequently, the calculated S value, obtained according to (22), is employed to assess the sensing performance. Fig. 10(b) illustrates the variation in the size of Q and FOM. The maximum values occur at 275 K, where $Q = 10569$ and FOM $= 0.073$ K^{-1}. Subsequently, there is a decline, reaching the lowest values at 350 K, with $Q = 5080.4$ and FOM $= 0.0351$ K^{-1}, therewith, a slight increase is observed at 375 K. The relationship between the maximum and minimum values, approximately two times, indicates that the T_{ext}-sensing performance indicators are somewhat unstable. Nonetheless, the values remain above 5000, which aligns with the anticipated T_{ext}-sensing performance.

The proposed ML demonstrates the capability to detect B. By uniformly increasing the B from 0 to 0.2 T, the transmission peak continuously shifts to the right, resulting

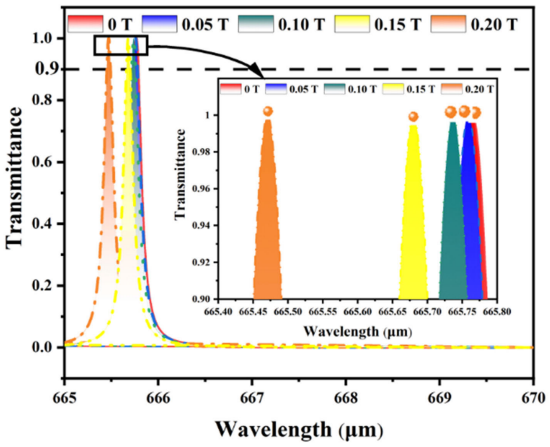

Fig. 11. Movement of transmission peaks is determined by different B.

in a crest shift of 0.294 μm. For visual clarity, an amplified view is denoted in Fig. 11. On the right side of the figure, it is obvious that the vertical coordinate of the peak remains closely aligned with a horizontal line at approximately 1. The peak data points are represented by orange stereo spheres. Specifically, the following peak wavelength values corresponding to different B are obtained, 0 T—665.765 μm, 0.05 T—665.759 μm, 0.10 T—665.737 μm, 0.15 T—665.681 μm, and 0.20 T—665.471 μm.

The heat map in Fig. 12(a) displays the transition from dark green to khaki, indicating the progression from low transmission to full transmission and stronger linear relationship are presented in Section 3 of Supplementary Material. The light-colored region in the figure stands for areas with transmittance greater than 0.8. Notably, as the B increases, the region with transmittance above 80% undergoes a gradual expansion, with a particularly pronounced bending effect observed around 0.15 to 0.20 T. Additionally, it can be observed that the movement rate of the peak wavelength during the initial growth of B is much smaller than in the later period. The initial movement is relatively gentle, whereas it becomes steeper later on. This variation in movement rate has an impact on the sensing performance S.

To assess whether S fulfills the requirements of sensing performance, the selected data points are plotted in a graph and subjected to linear fitting

$$\lambda = -1.332B + 665.8158. \tag{23}$$

The correlation coefficient R^2 remains consistently above 0.8, with a value of 0.8571, indicating a strong and negative correlation between B and peak wavelength. The slope, representing S, is calculated to be 1332 nm/T using (23). By inserting this value into (12) and (13), Q and FOM are computed for each selected data point, as depicted in Fig. 12(b). The average value of Q and FOM is determined to be 8146 and 16.3 T^{-1}, respectively. The overall trend reveals an initial increase in the maximum value, followed by a rapid decrease to the minimum value, and eventually a slight rise. The cumulative sum of Q amounts to 40 730, and FOM

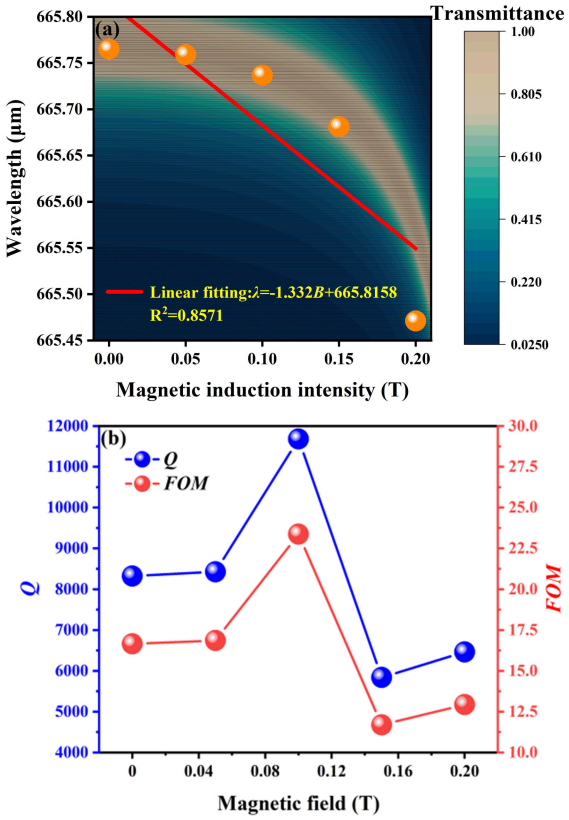

Fig. 12. (a) Heat map of B, peak operating wavelength, and transmittance. (b) Evaluation of B sensing performance.

reaches 81.5 T^{-1}, signifying that the sensing performance of the B aligns with the application standard.

The proposed ML demonstrates the capability of ultrawide range RI measurement, marking one of the major highlights of this article. In the realm of physical knowledge, with the exception of nearly 0 RI materials, negative RI materials, and ceramic materials with high dielectric constants [47], [48], [49], the RI of most materials lies within the range of 1 to 5, regardless of their state—solid, liquid, or gas. The ML presented in this study covers the entire measurement range. Fig. 13 showcases the distribution of transmittance at various RI values. Dark red indicates full transmittance, dark blue represents zero transmittance, and the color gradient from red to yellow to green to cyan to blue illustrates the gradual decrease in transmittance from 1 to 0 by increments of 0.8, 0.6, 0.4, and 0.2. In addition, it can be observed that the relationship between RI and the central working wavelength of the transmission peak is a straight line with a certain slope as a whole. For a more direct presentation, in Fig. 13, bright green, dark khaki, and bright red are divided into three straight lines with similar slopes, and the strong linear relationship corresponding to such values is in line with the needs of sensor functions

$$\lambda = \begin{cases} 46.9n_{\text{analyte}} + 618.9, & 1.0 \le n < 2.0 \\ 79.1n_{\text{analyte}} + 454.5, & 2.0 \le n < 3.5 \\ 106.1n_{\text{analyte}} + 459.9, & 3.5 \le n \le 5.0. \end{cases} \tag{24}$$

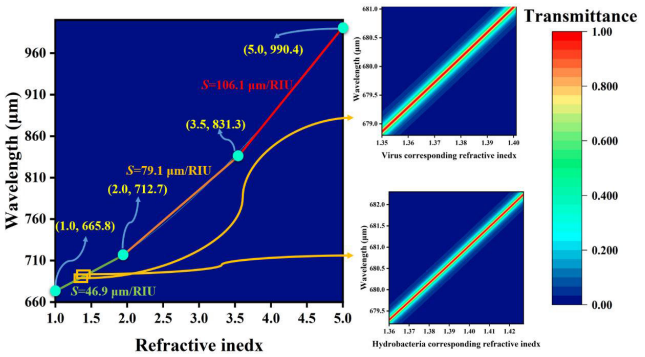

Fig. 13. Distribution of the transmittance of ML over the full RI.

TABLE II
RI OF THE UTILIZED VIRUS

Virus	Zero cancer cell	Jurkat	HeLa	PC12	MDA-MB-231	MCF-7
RI	1.350	1.390	1.392	1.395	1.399	1.401

Although the transmission peak curve appears narrow in the figure, the overall trend of change reveals a curve with a gradually increasing slope. To display the transmittance distribution more clearly, a bold line is employed to depict the curve of high transmittance. The entire RI measurement range is divided into three distinct detection ranges of S, determined by four data points, (1.0, 665.8), (2.0, 712.7), (3.5, 831.3), and (5.0, 990.4). The avocado-colored line represents a high S between RI 1 and 2, with a value of 4.69×10^4 nm/RIU. The reddish-orange line denotes an approximately straight curve at RI 2 to 3.5, exhibiting an S value of 7.91×10^4 nm/RIU. For the remaining range, the vermilion line illustrates $S = 1.061 \times 10^5$ nm/RIU. It can be observed that as the RI increases, the slope gradually rises, indicating that S consistently increases, maintaining a strong linear positive correlation. Thanks to the utilization of an air layer and Psi, the analyte can be conveniently filled, enhancing the measurement function of the ML, and making it more intuitive and convenient. The article lists the detection functions of hydrobacteria and viruses. On the right side of Fig. 13, a strong linear relationship can be observed between their corresponding RI and peak wavelength, which lays a foundation for displaying the sensing performance.

The findings of this study propose that ML holds promise for virus detection, emphasizing the significance of rapid and early detection in containing and preventing outbreaks effectively. Virus sensors demonstrate their ability to detect viruses across various sample types, such as air, water, and body fluids, facilitating timely response measures. The sample analysis layer in this research comprises an air layer and two distinct thicknesses of Psi, employed for the detection of six different viral cells. These observations contribute to advancing the field of virus detection and its potential applications in public health and disease control. The equivalent RI for each virus is detailed in Table II [50].

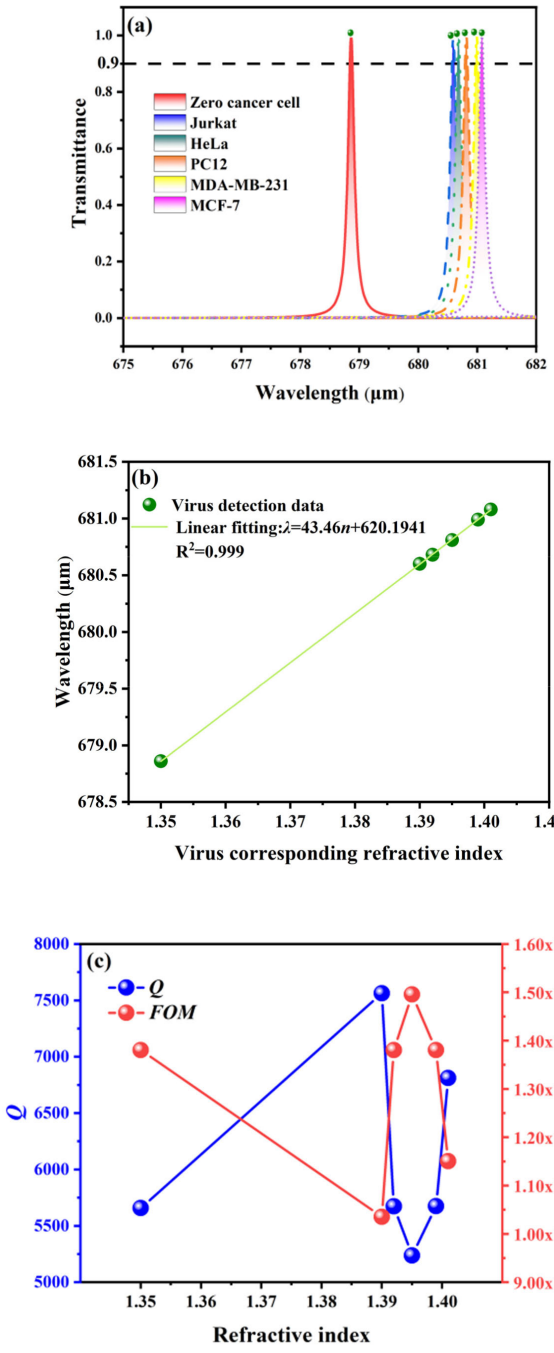

Fig. 14. (a) Influence of different viruses on the wavelength transmittance curve of the design structure. (b) Relationship between the change of types of viruses and wavelength of corresponding transmission peak. (c) Corresponding sensing performance values Q and FOM are obtained in the different types of viruses.

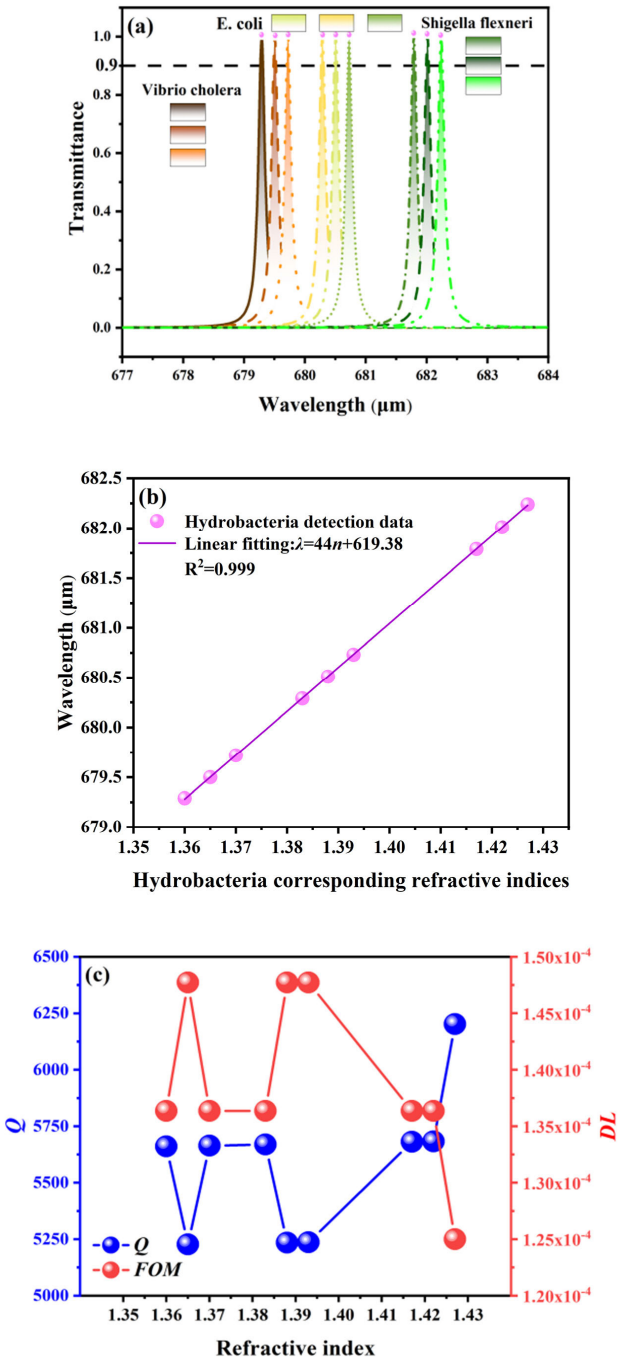

Fig. 15. (a) Transmittance of the three hydrobacteria within the working wavelength band is designed. (b) Curve relationship between wavelength of hydrobacteria and corresponding RI. (c) Sensing properties of the sensing are characterized by evaluating the Q and FOM.

TABLE III
RI OF THE UTILIZED HYDROBACTERIA

Hydrobacteria	E.coli	Shigella flexneri	Vibrio cholera
RI range	(1.383, 1.393)	(1.417, 1.427)	(1.360, 1.370)

The difference in analytes can be discerned based on the movement of the transmission peak. In Fig. 14(a), when analyzing zero cancer cells, the peak wavelength is observed at 678.86 μm. However, upon changing to the Jurkat virus, the transmission peak shifts to the right, measuring 680.6 μm. Moving further to the right, the green-white gradient curve at 680.68 μm represents the HeLa virus, the orange-white gradient filling curve at 680.81 μm corresponds to the PC12 virus, the peak wavelength is 680.99 μm for the MDA-MB-231 virus, and the pink-white gradient curve at the far right of the image represents MCF-7 virus, with the peak wavelength at 681.08 μm. It is evident that regardless of the type

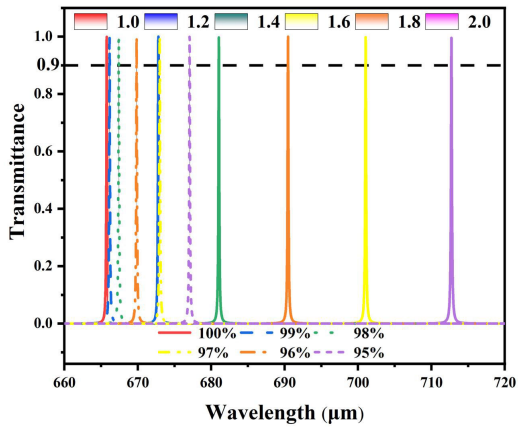

Fig. 16. Ideal and actual transmission spectra in the RI range of 1 ∼ 2.

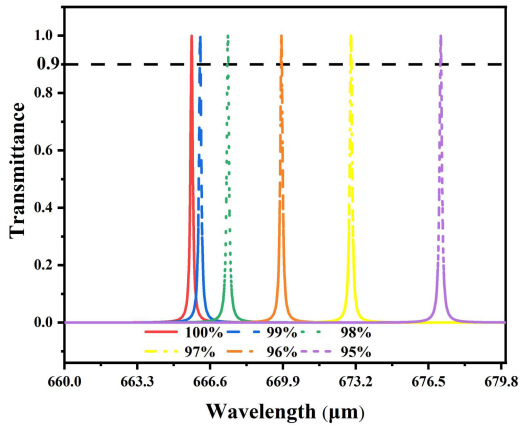

Fig. 17. Ideal and actual transmission spectra in the RI range of 1 ∼ 2.

of virus analyzed, the transmission peak undergoes a shift. To further investigate this relationship, the peak data points are extracted using green stereo balls for function fitting, yielding a positive correlation linear relationship with an impressively high correlation coefficient of 0.999, as depicted in Fig. 14(b)

$$\lambda = 43.46 n_{\text{virus}} + 620.1941. \tag{25}$$

The value of S, calculated as 4.346×10^4 using (25), plays a crucial role in the virus detection function of ML. As illustrated in Fig. 14(b), this figure directly displays the relationship between the corresponding RI of different viruses and the peak wavelength, demonstrating a strong linear correlation between the two variables. This fundamental relationship serves as the basis for the virus detection capability of ML. To assess the virus sensing performance, the value of S is incorporated into (12), (13), and (14), and the results are presented in Fig. 14(c). In evaluating the performance of a biosensor, the key indicators are Q and DL. Notably, Q and DL exhibit opposite trends with respect to the measured virus RI. As the RI of the virus increases, the Q value shows a slow rise from 5657 to the maximum value of 7562, followed by a rapid decline to the minimum value of 5237. Subsequently, it experiences varying rates of increase to reach 5675 and 6811. Conversely, the change in DL is entirely opposite. The overall mean of DL is calculated as 1.3×10^{-4}RIU, with a

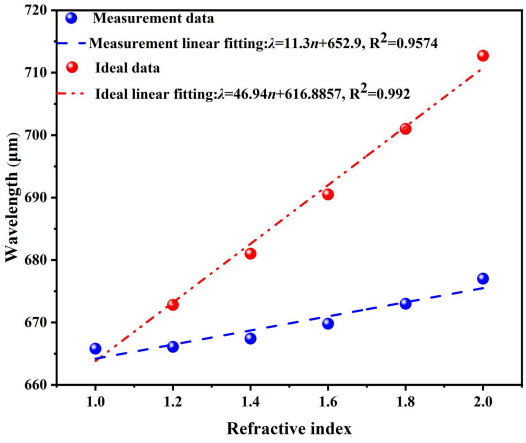

Fig. 18. Variation of RI in relation to ideal and actual transmission peak wavelength.

TABLE IV
PRIMARY USED MATERIALS AND METHODS

Materials and methods	Refs.
PFC	37
Insb	12
Psi	41
TMM	31
ACO	47

standard deviation of merely 1.732×10^{-5} RIU, satisfying the requirements for biosensing applications.

The proposed ML demonstrates the sensing characteristics of hydrobacteria, a critical aspect in safeguarding aquatic ecosystems and biodiversity. By detecting the levels of bacteria in water, it becomes feasible to assess their impact on the environment, thereby aiding conservation efforts and preserving ecological balance. The ability of ML to detect and analyze hydrobacteria is based on RI sensing and therefore requires the hydrobacteria and corresponding RI shown in Table III, and the materials and methods can be seen in Table IV [51].

In response to a range of RI, E.coli, Shigella flexneri, and Vibrio cholera were investigated to observe the sensing characteristics of the transmission peaks. The specific outcomes are illustrated in Fig. 15(a). When the RI values for E.coli are 1.383, 1.388, and 1.393, the corresponding transmission peak wavelengths are 680.29, 680.51, and 680.73 μm, respectively, distributed within the intermediate regions of the images. Similarly, for Vibrio cholera, the RI values of 1.360, 1.365, and 1.370 correspond to wavelength shifts from 679.29 to 679.72 μm, ultimately reaching 679.72 μm, as indicated by the predominant brown color. Moreover, the three peak wavelengths on the far right, predominantly green, at 681.79, 682.01, and 682.24 μm, signify the RI of Shigella flexneri. It is evident that the transmission peak wavelength exhibits a quasi-linear rightward shift with increasing RI, and the magnitude of the shift depends on the change in RI value.

For a more comprehensive and accurate exploration, the peak data points are subjected to fitting, and the results are

TABLE V
SENSING PERFORMANCE OF PUBLISHED REPORTS COMPARED WITH THIS ARTICLE

Reference	Multiple physical quantities detection	Analyte	Measuring range	Sensing performance			
				S	***Q***	***FOM***	***DL***
This work	✔	Thickness	7.34~7.54 μm	18.75	11885	332 μm^{-1}	✘
		T_{ext}	275~375 K	4.6 nm/K	7046	0.049 K^{-1}	✘
		B	0~0.2 T	1332 nm/T	8146	16.3 T^{-1}	✘
		RI	1~2	46900 nm/RIU	✘	✘	✘
			2~3.5	79100 nm/RIU	✘	✘	✘
			3.5~5	106100 nm/RIU	✘	✘	✘
		Virus	1.350~1.401	43460 nm/RIU	6103	✘	1.3×10^{-4}
		Hydrobacteria	1.383~1.370	44000 nm/RIU	5585	✘	1.38×10^{-4}
[52]	✘	RI	1.4~1.4028	1179 nm/RIU	1418	✘	2.2×10^{-5}
[53]	✘	Gas	1.35~1.4	450 nm/RIU	1105	800 RIU^{-1}	1.6×10^{-4}
[54]	✘	RI	1.330~1.345	900 nm/RIU	✘	0.013 RIU^{-1}	✘
[55]	✘	CH_4	1.34~1.37	550.08 nm/RIU	8.7	5.2 RIU^{-1}	✘
[56]	✘	RI	1~1.5	4784 nm/RIU	2149	1477 RIU^{-1}	✘
[57]	✘	RI	1.33~1.39	32000 nm/RIU	587.2	✘	4×10^{-4}
[58]	✘	RI	1.33~1.43	44000 nm/RIU	502	✘	1.6×10^{-3}
[59]	✗	Virus	1.350~1.401	72 nm/RIU	19	✗	✗
[60]	✗	Virus	1.33~1.43	42 nm/RIU	✗	✗	✗
[61]	✗	Blood Plasma	1.340~1.417	51.49 nm/RIU	✗	✗	✗
[62]	✗	Virus	1.33~1.43	10000 CFU mL^{-1}	✗	✗	80

presented in Fig. 15(b)

$$\lambda = 44n_{\text{hydrobacteria}} + 619.38. \tag{26}$$

An S value of up to 4.4×10^4 nm/RIU is obtained, and a correlation coefficient R^2 of up to 0.999 is achieved by fitting the pink data points, providing compelling evidence of a strong linear positive correlation between the RI corresponding to hydrobacteria and the peak wavelength. These significant values are utilized to calculate the sensing performance indicators, resulting in the distribution curves of Q and DL values as depicted in Fig. 15(c). The mean values of Q and DL are found to reach 5585 and 1.38×10^{-4} RIU, respectively. The sum of the nine data points is 50259.4 and 1.25×10^{-3} RIU, respectively. The standard deviation of the analyzed data, after obtaining the average value, is 314.5 and 7.6×10^{-6} RIU. In comparison to the data from each discrete point, this standard deviation is remarkably small, indicating that the Q and DL values exhibit only slight fluctuations within the measured range, thereby showcasing a relatively stable state of sensing performance.

In real-time sensing measurements conducted with the developed prototype, the transmittance values at specific operating wavelengths may undergo changes correlated with the decrease in the Q factor, contingent upon the detected species. Multiple measurements are imperative to obtain a statistically distributed dataset, providing insights into the reproducibility of the proposed ML sensing structure, resulting in diminished R^2 values. It is noteworthy that, with the reduction in the Q value, the size of the FWHM does not exert an influence on the linear fitting outcomes of peak wavelength points. Consequently, this article primarily focuses on the impact of the diminished Q value on peak wavelength. Exploiting the resonant characteristics of the proposed ML structure, it exhibits a screening function for specific wavelengths. However, this feature introduces a shift under diverse operational conditions during sensor deployment. Due to this being a purely theoretical study, to streamline research development, this article takes RI sensing as an illustrative example, concentrating on the exploration within the RI value range of 1 to 2. Incrementally applying offsets of 0%, 0.1%,

0.2%, 0.3%, 0.4%, and 0.5% to the peak wavelength, the results are presented in Fig. 16.

In Fig. 16, the solid lines, colored in red, blue, orange, yellow, and purple, respectively, depict the transmission spectrum corresponding to an increase in RI from small to large values. Upon the introduction of disturbances ranging from 0% to 5%, the resulting shift in the transmission spectrum to the left is illustrated by the dashed lines of corresponding colors. This shift indicates a noteworthy change in the peak wavelength. To delve deeper into whether the relationship between the peak points aligns with the sensor's design requirements, further exploration is warranted.

Since the positions of the curves are stacked on the left side after different degrees of disturbance are added, the observation is fuzzy, so the transmission curves added with disturbance are drawn separately, and the results are shown in Fig. 17.

In Fig. 17, it can be found that as the disturbance degree increases from 0% to 5%, the wavelength range of the change of transmission curve gradually increases. Obviously, this increment will affect the linear change of sensing results, so the increase in disturbance degree will lead to the reduction of sensing performance. The peak data points need to be extracted for further processing.

In this study, transmission peak data points from Fig. 17 were extracted, and linear fitting was conducted, with specific results presented in Fig. 18. Notably, the ideal data exhibited higher S values compared to the disturbed data, measuring 46.94 and 11.3 μm, respectively. Additionally, a slight decrease in the correlation coefficient is observed, reducing from 0.992 to 0.9574. While the correlation between data points experienced a minor deterioration, it still maintained a high correlation, meeting the design requirements for sensor components. These findings suggest that during actual measurement processes, variations arising from diverse factors and measured objects may influence device performance. However, the sensing characteristics can be preserved, indicating that the surface-presented structure demonstrates robustness and sensing reproducibility.

To further demonstrate the sensing performance of the ML proposed in this article, comparisons are made with other optical sensors, as shown in Table V for details.

IV. Materials and Methods

The main materials and methods used in this article are shown in Table IV. All the materials and methods are based on references and have been demonstrated by experiments. The main simulation calculation software is MATLAB 9.8.0.1417392 (R2020a) Update 4.

V. Conclusion

In this study, a novel ML based on Insb intrinsic resonance, capable of detecting multiple physical quantities across a wide measurement range is proposed. The utilization of SHW generation results in a high transmittance peak surpassing 0.999, leading to a narrower and higher-quality transmission profile. The ML demonstrates excellent performance in thickness measurement, exhibiting a favorable performance index, $S = 18.75$, $Q = 11885$, FOM $= 332\ \mu\text{m}^{-1}$. Additionally, it showcases strong sensing capabilities for T_{ext} and B, with S values of 4.6 nm/K and 1332 nm/T, Q values of 7046 and 8146, and FOM values of 0.049 K^{-1} and 16.3 T^{-1}, respectively. The ML also proves to be highly effective in RI sensing, capable of detecting substances within the range of RI $1 \sim 5$. Validation experiments involving viral ($S = 43460$ nm/RIU, $Q = 6103$, DL $= 1.3 \times 10^{-4}$ RIU) and hydrobacteria ($S = 44000$ nm/RIU, $Q = 5585$, DL $= 1.38 \times 10^{-4}$ RIU) tests demonstrate the robustness and reliability of RI sensing. These outstanding achievements are primarily attributed to the remarkable optimization ability of IACO, which improves the existing ACO. The integration of TMM further enhances the efficiency in computing the attributes of ML. The significant potential of the proposed ML and its improved optimization approach, IACO, is anticipated to make valuable contributions across various scientific fields.

References

[1] A. Mir, A. Akjouj, E. H. El Boudouti, B. Djafari-Rouhani, and L. Dobrzynski, "Large omnidirectional band gaps and selective transmission in one-dimensional multilayer photonic structures," *Vacuum*, vol. 63, nos. 1–2, pp. 197–203, Jul. 2001.

[2] H. Chen et al., "Recent advances of low-dimensional materials in Mid- and far-infrared photonics," *Appl. Mater. Today*, vol. 21, Dec. 2020, Art. no. 100800.

[3] E. Yablonovitch, "Photonic band-gap structures," *J. Opt. Soc. Amer. B, Opt. Phys.*, vol. 10, no. 2, pp. 283–295, Feb. 1993.

[4] M. Bayindir, E. Cubukcu, I. Bulu, T. Tut, E. Ozbay, and C. M. Soukoulis, "Photonic band gaps, defect characteristics, and waveguiding in two-dimensional disordered dielectric and metallic photonic crystals," *Phys. Rev. B, Condens. Matter*, vol. 64, no. 19, Oct. 2001, Art. no. 195113.

[5] Z. Peng, X. Chen, Y. Fan, D. J. Srolovitz, and D. Lei, "Strain engineering of 2D semiconductors and graphene: From strain fields to band-structure tuning and photonic applications," *Light, Sci. Appl.*, vol. 9, no. 1, p. 190, Nov. 2020.

[6] M. Annadhasan, S. Basak, N. Chandrasekhar, and R. Chandrasekar, "Next-generation organic photonics: The emergence of flexible crystal optical waveguides," *Adv. Opt. Mater.*, vol. 8, no. 21, Sep. 2020, Art. no. 2000959.

[7] V. S. Chaudhary, D. Kumar, and S. Kumar, "SPR-assisted photonic crystal fiber-based dual-wavelength single polarizing filter with improved performance," *IEEE Trans. Plasma Sci.*, vol. 49, no. 12, pp. 3803–3810, Dec. 2021.

[8] M. Mohammadi, F. Habibi, M. Seifouri, and S. Olyaee, "Recent advances on all-optical photonic crystal analog-to-digital converter (ADC)," *Opt. Quantum Electron.*, vol. 54, no. 3, p. 192, Mar. 2022.

[9] J. Haus, *Optical Sensors: Basics and Applications*. Hoboken, NJ, USA: Wiley, Jan. 2010.

[10] G. Gauglitz, "Direct optical sensors: Principles and selected applications," *Anal. Bioanal. Chem.*, vol. 381, no. 1, pp. 141–155, Jan. 2005.

[11] R. V. Nair and R. Vijaya, "Photonic crystal sensors: An overview," *Prog. Quantum Electron.*, vol. 34, no. 3, pp. 89–134, May 2010.

[12] T. Zhang, D. Zhang, and H. F. Zhang, "Realization of double Fano resonances with an Insb-doped Fabry–Pérot cavity," *Results Phys.*, vol. 35, Apr. 2022, Art. no. 105417.

[13] A. Kumar, V. Kumar, B. Suthar, A. Bhargava, K. S. Singh, and S. P. Ojha, "Wide range temperature sensors based on one-dimensional photonic crystal with a single defect," *Int. J. Microw. Sci. Technol.*, vol. 2012, pp. 1–5, Aug. 2012.

[14] M. Al-Dossari, S. Awasthi, A. Mohamed, N. Abd El-Gawaad, W. Sabra, and A. Aly, "Bio-alcohol sensor based on one-dimensional photonic crystals for detection of organic materials in wastewater," *Materials*, vol. 15, no. 11, p. 4012, Jun. 2022.

[15] J. Cimek, N. Liaros, and S. Couris, "Experimental investigation of the nonlinear refractive index of various soft glasses dedicated for the development of nonlinear photonic crystal fibers," *Opt. Mater. Exp.*, vol. 7, no. 10, pp. 3471–3483, Sep. 2017.

[16] Z.-Q. Hui and J.-G. Zhang, "Wavelength conversion, time demultiplexing and multicasting based on cross-phase modulation and four-wave mixing in dispersion-flattened highly nonlinear photonic crystal fiber," *J. Opt.*, vol. 14, no. 5, Apr. 2012, Art. no. 055402.

[17] A. S. Desyatnikov et al., "Nonlinear photonic lattices in anisotropic nonlocal self-focusing media," *Opt. Lett.*, vol. 30, no. 8, p. 869, Apr. 2005.

[18] F. Azadpour and A. Bahari, "All-optical bistability based on cavity resonances in nonlinear photonic crystal slab-reflector-based Fabry–Pérot cavity," *Opt. Commun.*, vol. 437, pp. 297–302, Apr. 2019.

[19] V. Dangui, M. J. F. Digonnet, and G. S. Kino, "Laser-driven photonic-bandgap fiber optic gyroscope with negligible Kerr-induced drift," *Opt. Lett.*, vol. 34, no. 7, p. 875, Apr. 2009.

[20] J.-J. Li, Z.-Y. Li, and D.-Z. Zhang, "Second harmonic generation in one-dimensional nonlinear photonic crystals solved by the transfer matrix method," *Phys. Rev. E, Stat. Phys. Plasmas Fluids Relat. Interdiscip. Top.*, vol. 75, no. 5, May 2007, Art. no. 056606.

[21] P. Chen et al., "Quasi-phase-matching-division multiplexing holography in a three-dimensional nonlinear photonic crystal," *Light, Sci. Appl.*, vol. 10, no. 1, p. 146, Jul. 2021.

[22] C. Li et al., "Three-dimensional nonlinear photonic crystal in naturally grown potassium–tantalate–niobate perovskite ferroelectrics," *Light: Sci. Appl.*, vol. 9, no. 1, p. 193, Nov. 2020.

[23] A. S. Aleksandrovsky, A. M. Vyunishev, A. I. Zaitsev, A. V. Zamkov, and V. G. Arkhipkin, "Detection of randomized nonlinear photonic crystal structure in a non-ferroelectric crystal," *J. Opt. A, Pure Appl. Opt.*, vol. 9, no. 9, pp. S334–S338, Aug. 2007.

[24] C. Pacholski, "Photonic crystal sensors based on porous silicon," *Sensors*, vol. 13, no. 4, pp. 4694–4713, Apr. 2013.

[25] G. A. Rodriguez et al., "Photonic crystal nanobeam biosensors based on porous silicon," *Opt. Exp.*, vol. 27, no. 7, p. 9536, Apr. 2019.

[26] M. S. Salem, M. J. Sailor, F. A. Harraz, T. Sakka, and Y. H. Ogata, "Electrochemical stabilization of porous silicon multilayers for sensing various chemical compounds," *J. Appl. Phys.*, vol. 100, no. 8, Oct. 2006, Art. no. 083530.

[27] M. Dorigo, M. Birattari, and T. Stutzle, "Ant colony optimization," *IEEE Comput. Intell. Mag.*, vol. 1, no. 4, pp. 28–39, Nov. 2006.

[28] M. Dorigo and G. Di Caro, "Ant colony optimization: A new meta-heuristic," in *Proc. Congr. Evol. Computation (CEC)*, Jul. 1999, pp. 1470–1477.

[29] M. Yousefikhoshbakht, F. Didehvar, and F. Rahmati, "An efficient solution for the vrp by using a hybrid elite ant system," *Int. J. Comput. Commun. Control*, vol. 9, no. 3, pp. 340–347, Apr. 2014.

[30] T. Stützle and M. Dorigo, "A short convergence proof for a class of ant colony optimization algorithms," *IEEE Trans. Evol. Comput.*, vol. 6, no. 4, pp. 358–365, Aug. 2002.

[31] A. H. Aly and H. A. Elsayed, "Defect mode properties in a one-dimensional photonic crystal," *Phys. B, Condens. Matter*, vol. 407, no. 1, pp. 120–125, Jan. 2012.

[32] A. Madani and S. R. Entezar, "Optical properties of one-dimensional photonic crystals containing graphene sheets," *Phys. B, Condens. Matter*, vol. 431, pp. 1–5, Dec. 2013.

[33] A. Miao, G. Chen, C. Yan, and Y. Wu, "Path planning optimization of an indoor mobile robot based on adaptive ant colony algorithm," *Comput. Ind. Eng.*, vol. 156, Jun. 2021, Art. no. 107230.

[34] J. Xu, Z. Tang, Y. R. Wu, and H. F. Zhang, "A multi-physical quantity sensor based on a layered photonic structure containing layered graphene hyperbolic metamaterials," *Phys. Chem. Chem. Phys.*, vol. 25, no. 26, pp. 17558–17570, Jul. 2023.

[35] F. Intonti et al., "Rewritable photonic circuits," *Appl. Phys. Lett.*, vol. 89, no. 21, Nov. 2006, Art. no. 211117.

[36] B. K. Teo and X. H. Sun, "Silicon-based low-dimensional nanomaterials and nanodevices," *ChemInform*, vol. 38, no. 32, pp. 1454–1532, Aug. 2007.

[37] D. Jafari, T. Nurmohammadi, M. J. Asadi, and K. Abbasian, "All-optical analog-to-digital converter based on Kerr effect in photonic crystal," *Opt. Laser Technol.*, vol. 101, pp. 138–143, May 2018.

[38] J. Gregório, S. Parsons, and J. Hopwood, "Reconfigurable photonic crystal using self-initiated gas breakdown," *Plasma Sources Sci. Technol.*, vol. 26, no. 2, Jan. 2017, Art. no. 02LT03.

[39] A. Kumar, V. Kumar, B. Suthar, M. Ojha, Kh. S. Singh, and S. P. Ojha, "Trapping of light in nonlinear 1-D photonic crystal," *IEEE Photon. Technol. Lett.*, vol. 25, no. 3, pp. 279–282, Feb. 2013.

[40] B. D. Salzberg and J. J. Villa, "Infrared refractive indexes of silicon germanium and modified selenium glass," *J. Opt. Soc. Amer.*, vol. 47, no. 3, pp. 244–246, Mar. 1957.

[41] P. Monk, *Finite Element Methods for Maxwell's Equations*. London, U.K.: Oxford Univ. Press, Apr. 2003.

[42] C. Yang, C. Guo, C. Peng, and H. Zhang, "Second harmonic generation in 1D nonlinear plasma photonic crystals," *Annalen der Physik*, vol. 535, no. 9, Jul. 2023, Art. no. 2300190.

[43] B.-F. Wan, Y. Xu, Z.-W. Zhou, D. Zhang, and H.-F. Zhang, "Theoretical investigation of a sensor based on one-dimensional photonic crystals to measure four physical quantities," *IEEE Sensors J.*, vol. 21, no. 3, pp. 2846–2853, Feb. 2021.

[44] B.-F. Wan, Q.-Y. Wang, H.-M. Peng, H.-N. Ye, and H.-F. Zhang, "A late-model optical biochemical sensor based on OTS for methane gas and glucose solution concentration detection," *IEEE Sensors J.*, vol. 21, no. 19, pp. 21465–21472, Oct. 2021.

[45] Q. Luo, H. Wang, and J. He, "Research on path planning of a mobile robot based on improved ant colony algorithm," *Neural Comput. Appl.*, vol. 32, pp. 1555–1566, Apr. 2020.

[46] L. Chen, X.-H. Xu, and Y.-X. Chen, "An adaptive ant colony clustering algorithm," in *Proc. Int. Conf. Mach. Learn. Cybern.*, Apr. 2021, pp. 1387–1392.

[47] I. Liberal and N. Engheta, "Near-zero refractive index photonics," *Nature Photon.*, vol. 11, no. 3, pp. 149–158, Mar. 2017.

[48] D. R. Smith, J. B. Pendry, and M. C. K. Wiltshire, "Metamaterials and negative refractive index," *Science*, vol. 305, no. 5685, pp. 788–792, 2004.

[49] C. Zhu, Z. Cai, X. Cao, Z. Fu, L. Li, and X. Wang, "High-dielectric-constant nanograin $BaTiO_3$-based ceramics for ultra-thin layer multilayer ceramic capacitors via grain grading engineering," *Adv. Powder Mater.*, vol. 1, no. 3, Jul. 2022, Art. no. 100029.

[50] P. Sharan, S. M. Bharadwaj, F. Dackson Gudagunti, and P. Deshmukh, "Design and modelling of photonic sensor for cancer cell detection," in *Proc. Int. Conf. IMpact E-Technol. U.S. (IMPETUS)*, Jan. 2014, pp. 20–24.

[51] P. Y. Liu et al., "An optofluidic imaging system to measure the biophysical signature of single waterborne bacteria," *Lab Chip*, vol. 14, no. 21, pp. 4237–4243, 2014.

[52] Y. Chen, J. Dong, T. Liu, Q. Zhu, and W. Chen, "Refractive index sensing performance analysis of photonic crystal containing graphene based on optical Tamm state," *Modern Phys. Lett. B*, vol. 30, no. 4, Feb. 2016, Art. no. 1650030.

[53] X. Qian, Y. Zhao, Y.-N. Zhang, and Q. Wang, "Theoretical research of gas sensing method based on photonic crystal cavity and fiber loop ring-down technique," *Sens. Actuators B, Chem.*, vol. 228, pp. 665–672, Jun. 2016.

[54] R. Das, T. Srivastava, and R. Jha, "On the performance of tamm-plasmon and surface-plasmon hybrid-mode refractive-index sensor in metallo-dielectric heterostructure configuration," *Sens. Actuators B, Chem.*, vol. 206, pp. 443–448, Jan. 2015.

[55] H. Liu, C. Chen, Y. Zhang, B. Bai, and S. Tang, "A high-sensitivity methane sensor with localized surface plasmon resonance behavior in an improved hexagonal gold nanoring array," *Sensors*, vol. 19, no. 21, p. 4803, Nov. 2019.

[56] A. M. Ahmed and A. Mehaney, "Ultra-high sensitive 1D porous silicon photonic crystal sensor based on the coupling of Tamm/Fano resonances in the mid-infrared region," *Sci. Rep.*, vol. 9, no. 1, p. 6973, May 2019.

[57] M. R. Islam et al., "Design and numerical analysis of a gold-coated photonic crystal fiber based refractive index sensor," *Opt. Quantum Electron.*, vol. 53, no. 2, pp. 1–18, Feb. 2021.

[58] X. Chen, L. Xia, and C. Li, "Surface plasmon resonance sensor based on a novel D-shaped photonic crystal fiber for low refractive index detection," *IEEE Photon. J.*, vol. 10, no. 1, pp. 1–9, Feb. 2018.

[59] A. Bijalwan, B. K. Singh, and V. Rastogi, "Analysis of one-dimensional photonic crystal based sensor for detection of blood plasma and cancer cells," *Optik*, vol. 226, Jan. 2021, Art. no. 165994.

[60] N. R. Ramanujam et al., "Enhanced sensitivity of cancer cell using one dimensional nano composite material coated photonic crystal," *Microsyst. Technol.*, vol. 25, no. 1, pp. 189–196, Jan. 2019.

[61] H. J. El-Khozondar, P. Mahalakshmi, and R. J. El-Khozondar, "Design of one-dimensional refractive index sensor using ternary photonic crystal waveguide for plasma blood samples applications," *Phys. E, Low-Dimensional Syst. Nanostruct.*, vol. 111, pp. 29–36, Jul. 2019.

[62] T. Bu, Q. Huang, and L. Yan, "Applicability of biological dye tracer in strip biosensor for ultrasensitive detection of pathogenic bacteria," *Food Chem.*, vol. 274, pp. 816–821, Feb. 2019.

Jie Xu was born in Nanjing, China, in 2003. He is currently pursuing the bachelor's degree with the College of Electronic and Optical Engineering and the College of Flexible Electronics (Future Technology), Nanjing University of Posts and Telecommunications, Nanjing, China.

His main research interests include sensors, polarization converters, and optimization algorithms.

Chu-Ming Guo was born in Jiangsu, China, in 2003. He is currently pursuing the bachelor's degree with the College of Electronic and Optical Engineering and the College of Flexible Electronics (Future Technology), Nanjing University of Posts and Telecommunications, Nanjing, China.

His main research interests include nonlinear metastructure, second harmonic generation, and second harmonic applications.

Cheng Yang was born in Guizhou, China, in 2003. He is currently pursuing the bachelor's degree with the College of Electronic and Optical Engineering and the College of Flexible Electronics (Future Technology), Nanjing University of Posts and Telecommunications, Nanjing, China.

His main research interests include second harmonic generation, liquid crystal metastructure, and electromagnetic detection.

Hai-Feng Zhang was born in Jiangxi, China, in 1978. He received the M.Sc. degree in electronics science and technology from Nanchang University, Nanchang, China, in 2008, and the Ph.D. degree from the College of Electronic and Information Engineering, Nanjing University of Aeronautics and Astronautics, Nanjing, China, in 2014.

He is currently working as a Professor at the College of Electronic and Optical Engineering and the College of Flexible Electronics (Future Technology), Nanjing University of Posts and Telecommunications, Nanjing. His main research interests include computational electromagnetics, plasma photonic crystals, sensors, and plasma stealthy and electromagnetic properties of metamaterials.